Biosensors and Bioelectronics: X 27 (2025) 100673

Contents lists available at ScienceDirect

Biosensors and Bioelectronics: X

journal homepage: www.journals.elsevier.com/biosensors-and-bioelectronics-x

Field-effect transistor for biosensing applications using a graphene channel with amine-rich coatings

Trung T. Pham [a,b,*], Jean-François Colomer [a], José Ignacio Veytia-Bucheli [c], Benjamin Ledoux [d], Henri-François Renard [d,e], Cédric R. Vandenabeele [a,b], Laurent Houssiau [a], Laurent A. Francis [f], Stéphane P. Vincent [c], Robert Sporken [a]

[a] Namur Institute of Structured Matter (NISM), Department of Physics, University of Namur, 61 Rue de Bruxelles, B-5000 Namur, Belgium
[b] Innovative Coating Solution S.A., Rue Jean Sonet 10, B-5032 Isnes, Belgium
[c] CBO, Department of Chemistry, University of Namur, 61 Rue de Bruxelles, B-5000 Namur, Belgium
[d] Morph-Im Platform, University of Namur, 61 Rue de Bruxelles, B-5000 Namur, Belgium
[e] Namur Research Institute in Life Sciences (NARILIS), Research Unit in Cell Biology, University of Namur, 61 Rue de Bruxelles, B-5000 Namur, Belgium
[f] ICTEAM Institute, Department of Electrical Engineering, UCLouvain, Belgium

ARTICLE INFO

Keywords:
Graphene
LG-GFET
Plasma polymerization
Biosensors
Cyclopropylamine

ABSTRACT

Since graphene has a unique band structure with the valence and conduction bands touching each other at a single point called the Dirac point, this makes it extremely sensitive to the surroundings such as doping, external electric field, mechanical deformation, etc. Hence, it is very desirable for sensing applications. However, its surface inertness poses significant drawbacks. Therefore, it is necessary to treat the graphene surface to bind biomolecules. In this paper, we report the use of amine-functionalized graphene by plasma polymerization to detect the presence of biomolecules in graphene channel based on a liquid-gate field-effect transistor (LG-GFET). Taking streptavidin and biotin as an example, the binding interactions of streptavidin–biotin complexes are detected by monitoring the shift of the Dirac point. By varying the streptavidin concentrations from 0.1 nM to 1000 nM, we found that our LG-GFET achieves detection capabilities as low as 0.1 nM. Our approach can be applied for the detection of biological molecules with low detection limit, high sensitivity, and stability.

1. Introduction

Graphene is a two-dimensional sheet of carbon atoms arranged in a hexagonal lattice. It has unique properties such as extremely high mechanical strength, electrical and thermal conductivity, and chemical stability (Geim and Novoselov, 2007; Yan et al., 2012). Because graphene is only one atomic layer thick, it is extremely sensitive to its surrounding environment. Electrons can be transferred to or from graphene, making it an ideal candidate for the detection of a wide range of molecules in gases (e.g. gas sensors) or liquids (e.g. biosensors) since its electrical conductivity will vary with physicochemical changes upon adsorption of molecules on the surface.

Among the different types of biosensors (Pourmadadi et al., 2022), graphene based field-effect transistor (GFET) devices have received considerable attention due to their simple and label-free operation (Fu et al., 2017; Novodchuk et al., 2021). To produce sensors, graphene must be deposited on an insulating substrate and electrical contacts must be established. Therefore, graphene is usually transferred from its original substrate (e.g. chemical vapor deposition (CVD) graphene on copper) onto an insulating one (e.g. SiO_2/Si) with a lift-off technique. The graphene surface is then modified with a bioreceptor that can recognize and bind a given biological target. This binding interaction provides the electric field that modifies the charge carrier concentration in the channel. An additional electric field can be applied from an isolated gate electrode on the backside or by applying a potential to the fluid layer containing the biological targets, used as a liquid gate. In such GFET the channel conductance can be either n-type or p-type, depending on the applied gate voltage. The transition between the two regions corresponds to minimum conductance; it occurs when the Fermi level crosses the Dirac point. Adsorption of biomolecules is detected either through measurement of the current through the graphene channel for a given gate voltage, or by measuring the shift of the Dirac point.

* Corresponding author at: Namur Institute of Structured Matter (NISM), Department of Physics, University of Namur, 61 Rue de Bruxelles, B-5000 Namur, Belgium.
E-mail address: trung.phamthanh@unamur.be (T.T. Pham).

https://doi.org/10.1016/j.biosx.2025.100673
Received 15 June 2025; Received in revised form 7 August 2025; Accepted 7 August 2025
Available online 2 September 2025

There are numerous reports about biosensors based on graphene including graphene oxide (GO), reduced graphene oxide (rGO), exfoliated graphene and CVD graphene. GO and rGO based FET or exfoliated graphene have been used for the detection of proteins, bacteria, and DNA (Ohno et al., 2009; Mohanty and Berry, 2008; Cai et al., 2014). However, the lateral size of graphene layers (typically several 100 nm) limits their applicability towards large-scale and graphene-based devices. CVD-grown graphene is more reproducible and can be obtained with larger size, but its surface inertness causes significant obstacles to practical applications. Therefore, it must be chemically treated to generate active groups for the binding of biomolecules. Non-covalent functionalization of graphene (Xu et al., 2018; Jeon et al., 2020; Zhou et al., 2017) based simply on π-π conjugation, is unstable and prone to washout, resulting in poor sensor reliability. Therefore, covalent functionalization is preferable, but often leads to significant damage to graphene in chemical solutions (Liu et al., 2012; Shown and Ganguly, 2016; Georgakilas et al., 2012). To avoid this problem, noble metal nanoparticles (NP) such as gold or platinum deposited on graphene are widely used as binding sites due to their biocompatibility and well-known functionalization chemistry (Cai et al., 2015; Gao et al., 2016).

Wan et al. (2021) reported an application of bare graphene transferred onto SiO_2/Si substrate as GFET using solution as the top-gate electrode for the detection of ovarian cancer cells. Although the sensor demonstrates high-sensitivity, it is not selective, and the detection mechanism is unclear. Zhou et al. (2017) fabricated a liquid-gate GFET biosensor based on non-covalent modification of the graphene surface with a 1-pyrenebutyric acid N-hydroxysuccinimide ester decorated with anti-carcinoembryonic antigen. The detection limit for carcinoembryonic antigen was about 100 pg mL^{-1} in phosphate buffered saline (PBS) solution. Similar work was reported by Kim et al. (2018) about the detection of alpha-fetoprotein (AFP) in hepatocellular carcinoma plasma and in PBS solution using a liquid-gate GFET based on non-covalent functionalization with 1-pyrenebutyric acid N-hydroxysuccinimide ester for immobilization of an anti-AFP antibody. Another group showed the detection of breast cancer cells by back-gated GFET decorated with Pt NP functionalized with HER3-specific scFv antibodies. The limit of detection is approximately 300 ng mL^{-1} in PBS (Gao et al., 2016). A similar concept based on FET configuration was developed using r-GO encapsulated silicon oxide NP for the detection of cancer biomarker proteins (Myung et al., 2011).

One can see from the literature that both liquid-gate GFET (LG-GFET) and back-gate GFET (BG-GFET) can be used to detect biomolecules, but using LG-GFET has some advantages. Huang et al. (2015) found that electrons in the graphene channel have higher mobility in the case of LG-GFET (12,000 $cm^2V^{-1}s^{-1}$) compared to BG-GFET (4000 $cm^2V^{-1}s^{-1}$). In addition, LG-GFETs can be easily controlled within a range of a few volts (−0.7 to +0.5 V for LG-GFET compared to −30 to +30 V for BG-GFET).

For biodetection, a major challenge comes from the fact that graphene surfaces are chemically inert. One needs to create different functional groups on graphene while preserving its structural quality. There are few known functionalization strategies that can achieve this with sufficiently strong bonding of the functional groups. We used plasma polymerization of cyclopropylamine (CPA) to deposit a thin, amine-rich ($-NH_2$) polymer film on graphene. We show that this coating provides reactive sites for covalent grafting of biomolecules via standard coupling chemistry, without degrading the electron or hole mobility. NHS ester-activated molecules readily react with the $-NH_2$ groups, forming stable amide bonds. In this study, we use the streptavidin–biotin interaction as a model system due to its high affinity and rapid kinetics. We demonstrate that our LG-GFET platform can sensitively detect streptavidin–biotin complexes at very low concentrations. This system not only validates our LG-GFET approach but also serves as a benchmark for future biosensor development.

2. Experimental details

Graphene was produced by atmospheric pressure chemical vapor deposition (APCVD) growth on copper foil and then transferred onto SiO_2/Si substrates as described in Ref. Pham et al. (2025). The crystalline and chemical quality of graphene after transfer was examined by Raman spectroscopy, X-ray photoelectron spectroscopy (XPS), and scanning electron microscopy (SEM). SEM observations were performed on the JEOL 6010LV. XPS analysis was made with a K-Alpha spectrometer from Thermo Scientific with a monochromatic Al Kα X-ray source (1486.6 eV). Raman scattering measurements were performed using a LabRAM Soleil HR system with a 532 nm laser excitation source and an objective of 100×.

GFETs were fabricated with 50 nm thick Au coating for source and drain electrodes deposited using a sputter coater (Quorum Q150T/ES). Oxygen plasma was applied with shadow mask to cut the graphene channel to the desired width (Pham et al., 2025). The drain - source current (I_D) was measured as a function of the gate–source voltage (V_{GS}) at a given source–drain voltage V_{DS} using a Keithley 2400 sourcemeter. The gate electrode was a Pt wire immersed in a droplet of electrolyte on the graphene channel.

Plasma polymerization of CPA was achieved in an inductively coupled plasma (ICP) discharge. The ICP discharge was generated from CPA (Merck, 99% purity) diluted or not in Ar gas (Air Liquide, 99.999% purity) in a 25 cm long, 10 cm in diameter quartz tube, juxtaposed to a vacuum chamber and wrapped with a copper coil powered with a 13.56 MHz RF plasma source (see the supplementary Figure S1). The whole vacuum system was evacuated to a base pressure lower than 1.0×10^{-4} mbar using a combination of a rotary pump and a turbo molecular pump. Bare SiO_2/Si substrate was exposed to plasma for about 30 s at 25 W forwarded power under three different conditions (10 sccm CPA + 10 sccm Ar, 20 sccm CPA + 10 sccm Ar, and 20 sccm CPA) to test the coating of polymerized films. The pressure during polymerization reaction was about 1.6×10^{-2} mbar without pressure regulation. The coating of CPA polymerized film is hereafter referred to as CPA-PPF (CPA-plasma polymer film).

Biotin (EZ-Link NHS-Biotin) and streptavidin (Alexa FluorTM 488 streptavidin) were ordered from Thermo Fisher Scientific. Biotin was dissolved in dimethyl formamide (DMF) while streptavidin was dissolved in PBS. A 2 mM NHS-Biotin solution was used to graft biotin molecules on the amine coated surface by continuous shaking for two hours at room temperature. Then, the samples were dried naturally at room temperature. Excess NHS-Biotin was rinsed off with DMF. Streptavidin was prepared in PBS solution (pH = 7.4) with different concentrations such as 0.1 nM, 0.2 nM, 0.5 nM, 1 nM, 10 nM, 100 nM, 200 nM, 500 nM, and 1000 nM. A micropipette was used to drop approximately 15 μl of solution for each measurement. After each experiment, the graphene channel was washed with PBS solution before next experiments (see next section).

Fluorescent samples were then imaged using a Zeiss LSM900 confocal laser scanning microscope equipped with a Plan Apo 63x, numerical aperture 1.4, oil immersion objective. Excitation was done at 488 nm and detection was measured at 490–600 nm. Laser power and PMT sensitivity were optimized on the most intense sample (to avoid signal saturation) and kept constant between the various experimental conditions of the same figure. So fluorescence intensities are quantitatively comparable.

3. Results and discussions

3.1. XPS analysis of different polymerization conditions

XPS analysis of CPA-PPF on SiO_2 prepared using the above three different conditions is shown in Fig. 1.

The coated films contain a strong N1s peak at 399 eV, which is attributed to amino groups (Artemenko et al., 2021). Its intensity depends

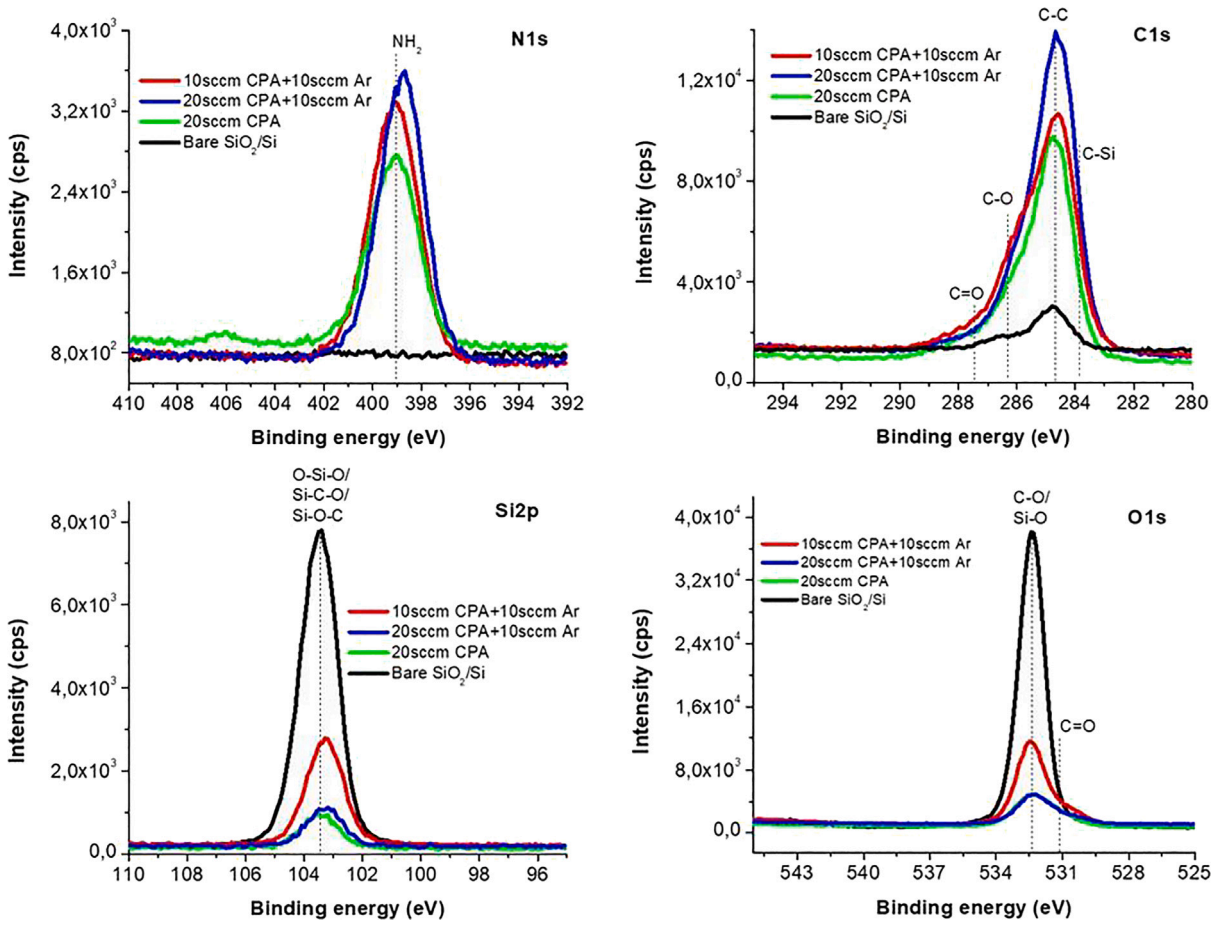

Fig. 1. XPS analysis of CPA-PPF on SiO_2/Si using three different conditions: 10 sccm CPA + 10 sccm Ar, 20 sccm CPA + 10 sccm Ar, and 20 sccm CPA. Bare SiO_2/Si is added as reference.

on the concentration of amines for different preparation conditions. A small peak at ~ 406 eV is observed in the sample without Ar plasma representing a satellite peak similar to nitrogen-containing aromatic polymers (e.g., polymide) due to weak $\pi - \pi$ interactions. It suggests that without Ar, plasma breaks less CPA molecules and so conserves the ring in CPA molecules. Si-O-C, Si-C-O and O-C bonds from O1s and Si2p are found mostly in the sample with 10 sccm CPA + 10 sccm Ar, indicating the covalent bonding between polymerized films and SiO_2 substrate. The C1s spectra show the peak shapes and intensities of the corresponding samples containing C–C, Si-C and O-C bonds compared to bare SiO_2/Si. So the best condition for the coating was 10 sccm CPA + 10 sccm Ar, where the CPA-PPF layer is thinner for this sample (cf. intensity of O-Si-O in Si 2p and O 1s) and more fragmented (cf. absence of satellite peak in *N* 1s). Thus, we selected this condition to produce different samples named as sample #1 (bare glass), sample #2 (CPA-PPF/glass), sample #3 (biotin/CPA-PPF/glass), sample #4 (fluorescent streptavidin/CPA-PPF/glass), sample #5 (non-fluorescent streptavidin/biotin/CPA-PPF/glass), and sample #6 (fluorescent streptavidin/biotin/CPA-PPF/glass) for fluorescence test. For this purpose, fluorescent streptavidin was prepared and incubated with samples #4, #5, and #6 at a concentration of 1000 nM. After 30 min of incubation, samples were rinsed several times with PBS and kept in PBS. Samples were then imaged in confocal microscopy. In theory, the fluorescence of streptavidin can be imaged if biotin is already immobilized on the surface through the reaction with amino groups at the surface, otherwise only diffuse background is observed.

3.2. Confocal imaging

Fig. 2(a) shows the confocal micrographs taken along with the extracted fluorescence intensity on the corresponding samples.

Fluorescence imaging reveals a strong signal on sample #6, indicating the presence of streptavidin on the surface. In contrast, other samples exhibit very weak fluorescence, primarily due to diffuse background noise. Using a consistent color scale across all images, sample #6 clearly shows the highest fluorescence intensity, attributable to the specific biotin–streptavidin interaction. By taking a height profile over the coating border (see the supplementary Figure S2), the thickness of the CPA-PPF films before biotin–streptavidin experiments was determined to be about 6 nm. The background signal observed in sample #4 may result from non-specific binding of fluorescent streptavidin to the surface.

3.3. SEM, Raman - XPS analysis

GFETs on SiO_2/Si substrates were fabricated with graphene channel coated CPA-PPF using the same condition as sample #6 and are shown in Fig. 3.

Fig. 3(a) shows the fabricated GFET on SiO_2/Si substrate within the transferred graphene over the channel between two Au electrodes. Fig. 3(b) shows the surface morphology of graphene on SiO_2 together with Raman spectrum recorded confirming the high quality of monolayer graphene with negligible D peak and the 2D/G peak ratio around 2. Small domains with darker contrast originate from the bilayer. Higher

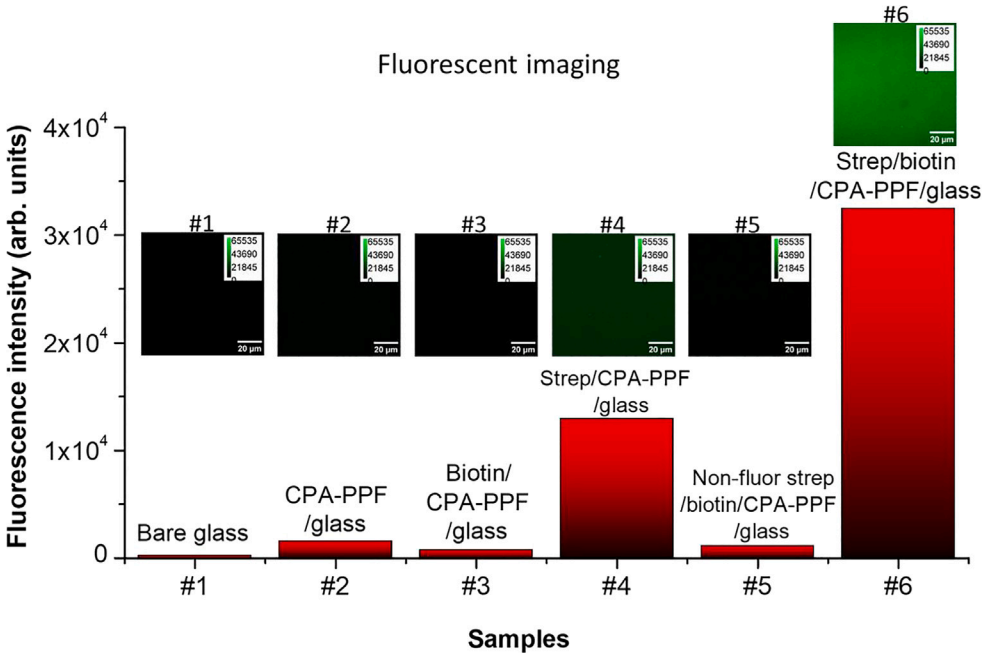

Fig. 2. Fluorescence intensity of different samples along with their corresponding micrographs.

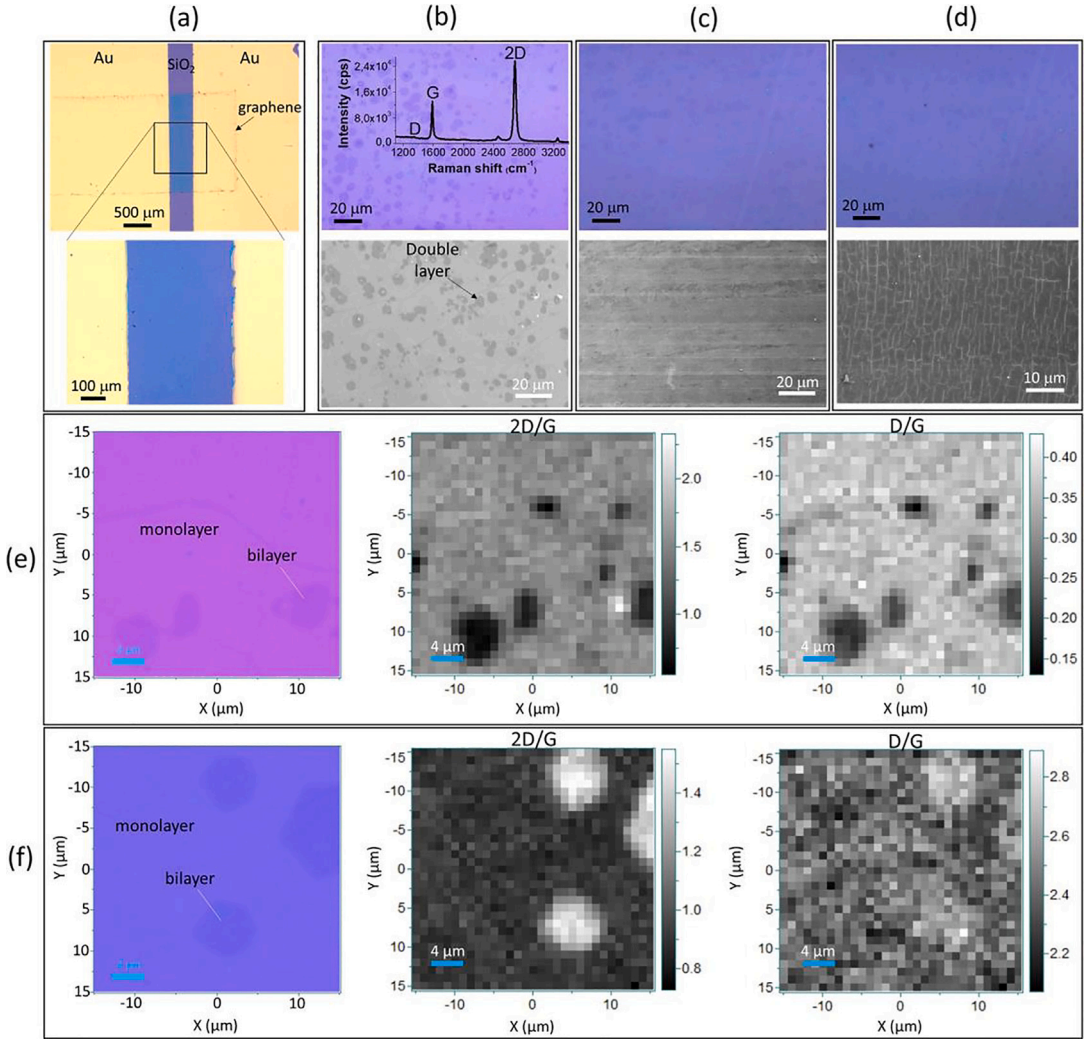

Fig. 3. Optical and SEM images: (a) the fabricated GFET on SiO_2/Si substrate with the graphene channel and Au electrodes, (b) bare graphene with small double-layer domains along with the Raman spectrum recorded showing high graphene quality, (c) the graphene surface after CPA-PPF coatings and, (d) the CPA-PPF surface after biotin reaction. Raman maps of 2D/G, and D/G: (e) bare graphene, (f) after CPA-PPF coatings.

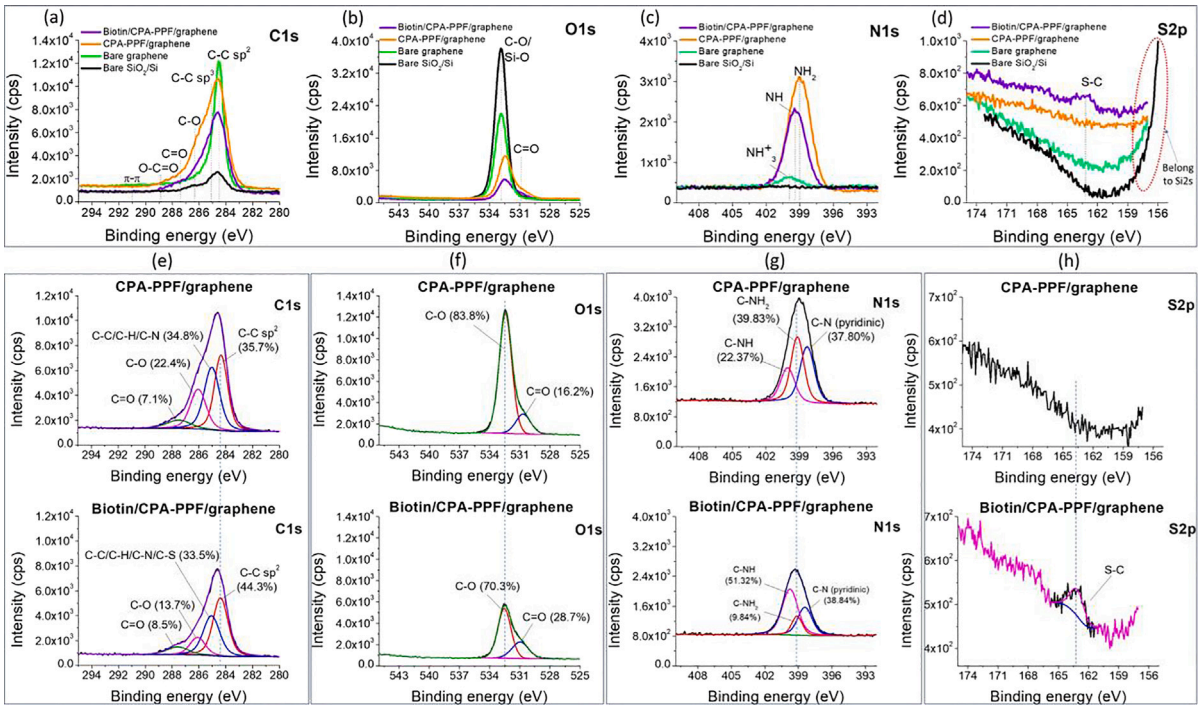

Fig. 4. XPS characterization of the sample after biotin reaction in comparison with other samples: (a) C1s, (b) O1s, (c) N1s, (d) S2p. Peak fittings: (e) C1s, (f) O1s, (g) N1s, and (h) S2p.

resolution with SEM is more clearly showing clean and continuous graphene on the SiO_2 substrate. After CPA polymerization (Fig. 3(c)), graphene surface is now covered with a thin CPA-PPF. Although the SEM images show a completely different surface morphology after CPA-PPF coatings, the underlying graphene can still be observed by optical microscope, meaning that the CPA-PPF is transparent at the given coating thickness. The CPA-PPF/graphene is embedded in dimethylformamide (DMF) within biotin-NHS. Interestingly, the surface morphology appears with porous-like structures after biotin reaction in Fig. 3(d). According to the schematic model in supplementary Figure S3, it is expected that the presence of the NHS-ester allows biotin coupling by the formation of an amide bond. The surface structure is mainly created by the presence of biotin after reaction with the amines.

Raman spectra were taken to check the quality of the graphene channel before and after CPA polymerization (supplementary Figure S4). A high defect concentration due to plasma polymerization can be observed. The D peak is very strong along with two other defect peaks marked by D'(1) and D'(2) at 1620 cm^{-2} and 2944 cm^{-2} respectively while those are absent in bare graphene before CPA-PPF coatings. Such defective graphene is very similar to those originated from nitrogen-doped graphene (Nam et al., 2024). The defect density is estimated using the formula characterized by Cançado et al. Cançado et al. (2011) about $5.3 \times 10^{11} cm^{-2}$ for both monolayer and bilayer graphene. To evaluate the defect distribution in graphene, Raman maps of 2D/G and D/G over a given graphene area before and after the CPA-PPF coating were performed and shown in Figs. 3 (e) & (f). The 2D/G ratio in monolayer graphene decreases from ~2 to ~1 after CPA-PPF coatings while the D/G ratio increases sharply from ~0.4 to ~2.6. The D/G map shows the similar contrast across the graphene defects, indicating the uniformity of the CPA-PPF coated graphene. This suggests that the generated defects probably play an important role as defect sites for the covalent bonding of the fragmented monomers with graphene films. Experimentally, the defect density in graphene can be controlled by adjusting the appropriate Ar ion flux at 25 W plasma power as provided in supplementary Figure S4.

As biotin contains sulfur (S), another XPS analysis was performed to detect S in Fig. 4.

Different samples were prepared such as bare SiO_2, graphene on SiO_2, CPA-PPF/graphene on SiO_2, and biotin/CPA-PPF/graphene on SiO_2. It was expected that the S2p spectrum (Fig. 4(d)) shows a peak at ~ 163 eV which is evidence of biotin-derived Sulfur in the biotin/CPA-PPF/graphene sample. The N1s peak (Fig. 4(c)) shifts about 0.6 eV to higher binding energy in the presence of biotin because primary amine ($-NH_2$) is converted into amide (-CONH-). This is consistent with our biotin NHS-amide model in the supplementary Figure S3. The decrease in N1s peak intensity after biotin reaction can be understood as due to the attenuation after biotin. Similar attenuation was also seen on other peaks like C1s (Fig. 4(a)), Si2p (supplementary Figure S5) and O1s (Fig. 4(b)) of the same sample to confirm the agreement between different elemental analyses. This suggests that biotin is well immobilized on the surface. The width of the C1s peak is larger after CPA-PPF coatings due to more carbon signals from fragmented CPA monomers along with the sp^2 C–C bonds of the underlying graphene. Similarly, the predominant C-O and C=O are mainly derived from biotin. The part of the S2p spectrum below 160 eV as marked is dominated by the tail from Si2s, not a sulfur signal.

Further details of the different components were resolved as detailed by the peak fittings shown in Figs. 4 (e-h). Different peaks of C1s such as C–C sp^2 bonds at ~284.4 eV, C–C/C-H/C-N or C-S (after biotin reaction) as sp^3 bonds at ~285.1 eV, C-O bonds at ~286.1 eV, and C=O bonds at ~287.5 eV. The C-O/C=O bond ratio in O1s decreased after reaction with biotin due to the presence of biotin containing more C=O bonds on the surface. Interestingly, N1s contains three different components with the main peak of amine at ~399 eV. The other peaks at ~398.4 eV and ~399.7 eV are attributed to C-N called pyridinic nitrogen (Vesel et al., 2020) and are characteristic of amide, respectively (Ravi et al., 2018). It can be seen that the amount of amines decreases rapidly and amides predominate after the biotin reaction. This explains the presence of biotin in the sample, where S2p exhibits an S-C bonds due to the covalent binding of biotin to amines on the surface.

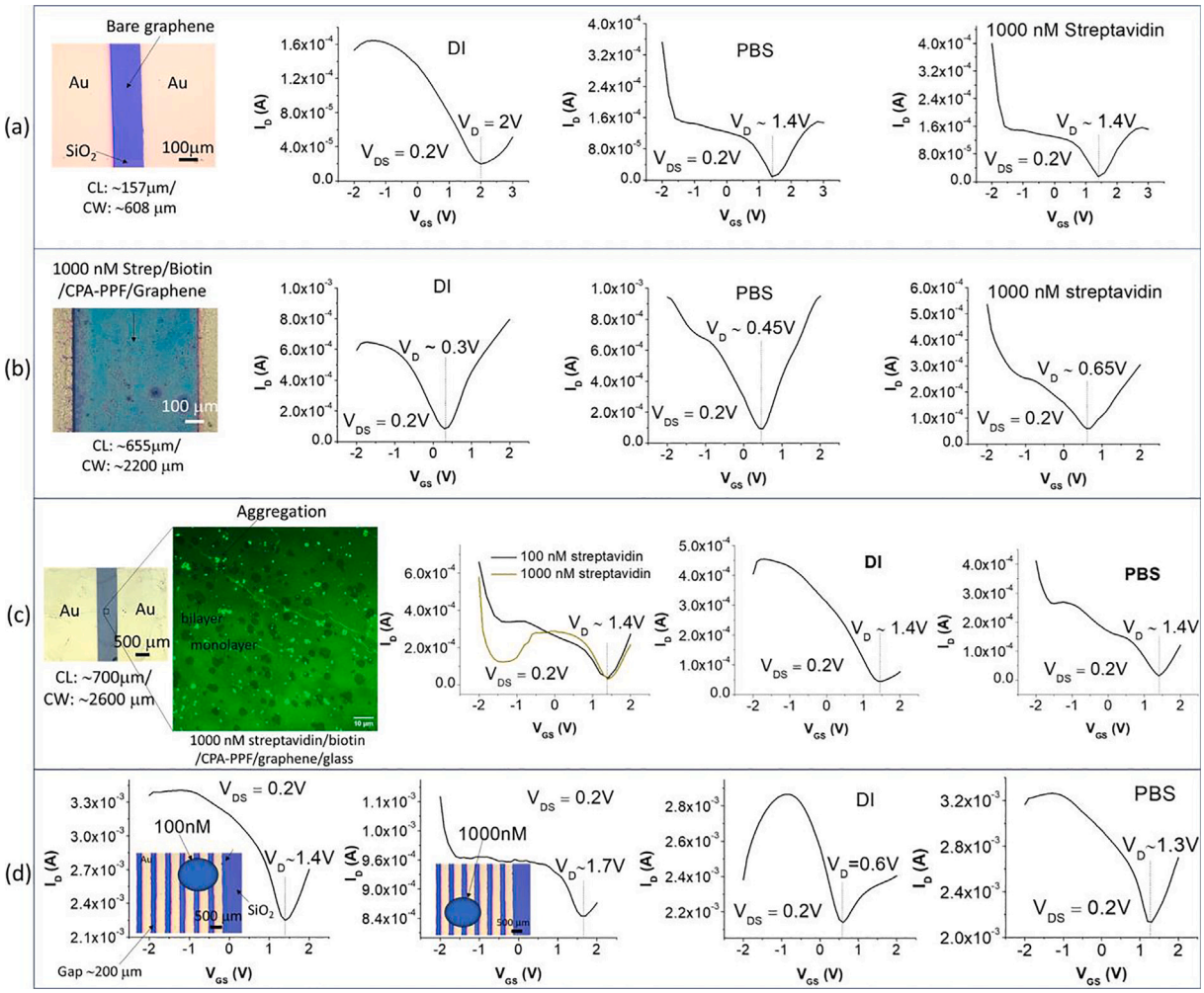

Fig. 5. The I–V characteristics of LG-GFET measured using three different electrolytes such as DI, PBS and streptavidin: (a) bare graphene/SiO_2/Si, (b) biotin/CPA-PPF/graphene/SiO_2/Si. (c) biotin/CPA-PPF/graphene on glass for confocal imaging prior to the I-V characterization. (d) biotin/CPA-PPF/graphene based comb-like electrodes/SiO_2/Si.

3.4. Electrical measurements

Electrical measurements were made using the setup shown in supplementary Figure S6 on bare graphene/SiO_2, and on biotin/CPA-PPF/graphene/SiO_2 with a liquid gate of deionized water (DI), PBS and streptavidin. PBS was used as the background to measure the signal of different concentration of streptavidin while DI was used to assess the difference in Dirac point position marked V_D between PBS and DI due to different molecular/ionic components (Wang and Burke, 2013). Indeed, Fig. 5(a) shows the I-V curves recorded on bare graphene measured with DI, PBS and 1000 nM streptavidin. The Dirac point position was determined $V_D \sim 2$ V for DI and $V_D \sim 1.4$ V for PBS at $V_{DS} = 0.2$ V. It is not surprising to see that the Dirac point of graphene does not change between PBS and streptavidin since graphene is non-reactive.

Using the same molecules, the behavior of Dirac point was examined on the biotin/CPA-PPF coated graphene in Fig. 5(b). Interestingly, there is a clear difference before and after streptavidin interaction. The Dirac point shifts by about 0.2 V with respect to the one of PBS, meaning that the conduction of the graphene channel is affected by the presence of streptavidin. The shift towards higher positive voltage indicates that electrons are transferred from graphene to streptavidin as p-type conductivity. The electron mobility is calculated ~ 90 cm^2 V^{-1} s^{-1} for bare graphene measured with PBS. This obtained value is similar to that reported in the literature (Cao et al., 2018) which is due to the high resistivity liquid. However, it is found more interesting for CPA-PPF/graphene with electron mobility ~ 2200 cm^2 V^{-1} s^{-1}, about 25 times larger than liquid/graphene. More details of our calculation model are added in Supplementary Figure S7.

To confirm the presence of streptavidin on the graphene channel, another identical GFET was prepared on glass with 1000 nM fluorescent streptavidin and imaged by confocal microscopy. The result is shown in Fig. 5 (c). The green color in the image refers to streptavidin along with some bright spots due to its aggregation and thus, the Dirac point was found at $V_D \sim 1.4$ V. So there is a correlation between 1000 nM streptavidin and V_D. By rinsing the graphene channel followed by measurements with 100 nM streptavidin, PBS and DI on the same sample, we found that the Dirac point position remained unchanged, suggesting that the surface was saturated with 1000 nM streptavidin. Remarkably, the two conductance minima occur as a double Dirac point at 1.4 V and −1.4 V measured at 1000 nM streptavidin. This phenomenon is similar to that observed in the back-gate GFET (Bartolomeo et al., 2011). This behavior arises from a combination of factors, primarily related to charge transfer and trapping at the graphene–electrode and graphene–dielectric interfaces because they probably alter the doping level of graphene, leading to changes in its conductivity and contributing to such double dip effects. In our case, this effect may be stronger due to the imperfection of the isolated CPA-PPF films at high concentration of streptavidin compared to BG-GFET.

Similarly, another GFET was tested in reverse by measuring first at 100 nM, then at 1000 nM. Both concentrations show almost the same

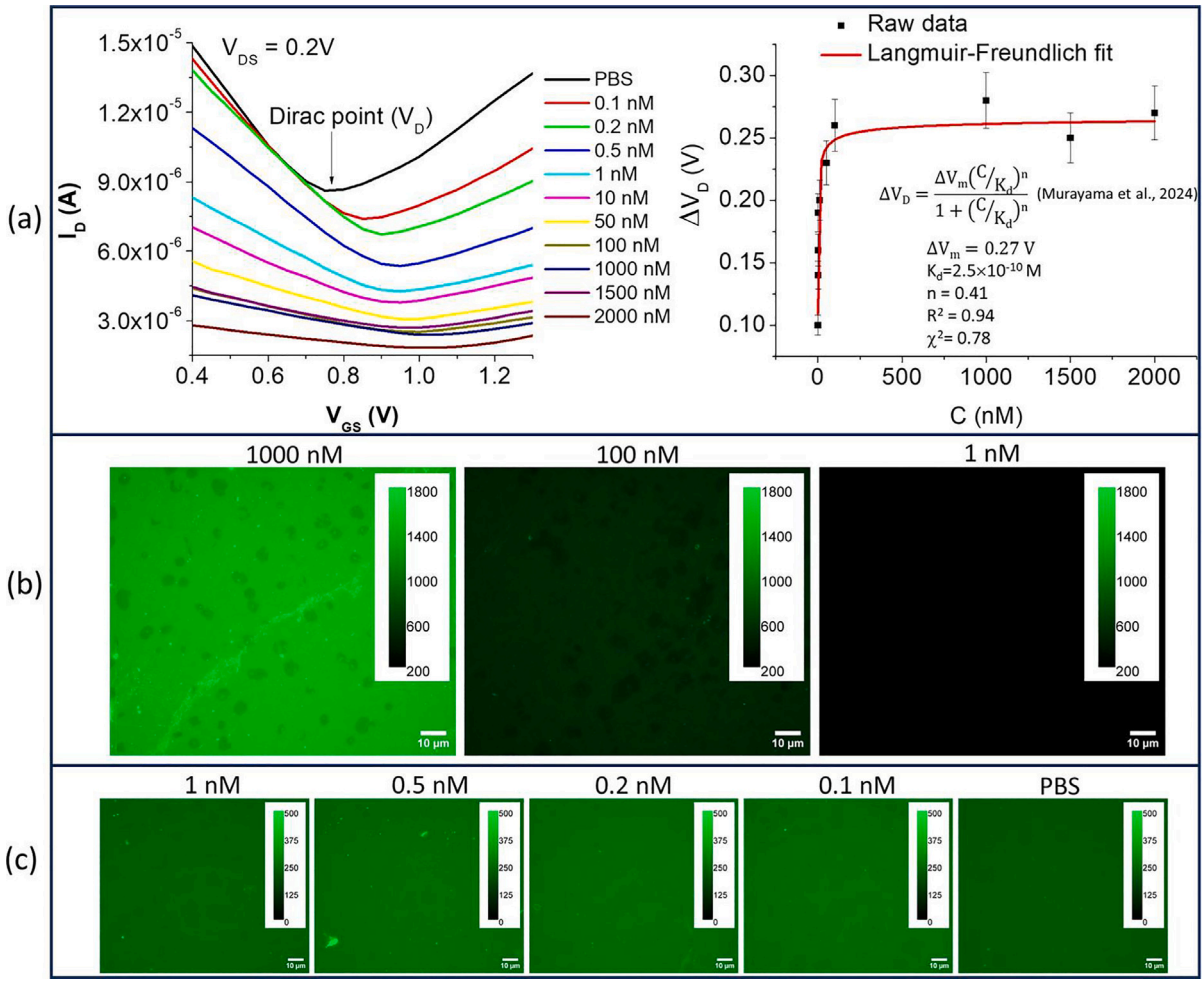

Fig. 6. (a) The I-V characteristics of LG-GFET (biotin/CPA-PPF/graphene/SiO_2/Si) using DI, PBS and fluorescent streptavidin at various concentrations along with the Dirac point shift vs. concentration. Confocal images of different fluorescent streptavidin concentrations: (b) Normal mode, (c) high sensitivity mode.

V_D at about 1.4 V as shown in supplementary Figure S8. It is possible that such concentrations used were too high due to the presence of too much streptavidin in the graphene channel or since the scanning window of V_{GS} was still large, so very small shift in the curve cannot be found.

To understand the effect of different concentrations on the Dirac point shift, a larger graphene channel was fabricated as comb-like electrodes (multichannel) in Fig. 5(d) to separate two droplets of two different concentrations on the same location as done above for the normal electrode (single channel). Otherwise, the graphene channel would saturate from one concentration before testing the other. By measuring on two different droplets like one drop for 100 nM at the location 1 and the other one for 1000 nM at the location 2, we found that the Dirac point shifted more at 1000 nM than at 100 nM, meaning that the shift of the Dirac point behaves as a function of streptavidin concentration. Spectra measured with DI and PBS respectively were added for comparison.

Further measurements were performed on another GFET using different concentrations of streptavidin from 0.1 nM to 1000 nM as shown in Fig. 6(a). Two additional concentrations at 1500 nM and 2000 nM were also prepared to test the saturation behavior during our GFET detection. Therefore, the shift of the Dirac point was carefully examined by starting at lowest concentration. The surface was rinsed with PBS and blown with nitrogen gas before starting with another concentration. Each measurement at a given concentration was done for about 30 s and repeated three different times. The first measurement with PBS was performed from −2 V to +2 V to determine the position of the Dirac point. The V_{GS} sweep was then reset as narrowly as possible around the Dirac point to monitor its behavior.

Compared with the Dirac point position measured with PBS (~ 0.76 V), it can be clearly seen that the Dirac point shifts up to 0.86 V at 0.1 nM streptavidin concentration. The position of Dirac point is determined by fitting the curve to allow for a more precise minimum current of the Dirac point. Then, 0.2 nM and 0.5 nM were measured in order showing their positions at about 0.90 V, 0.92 V respectively. Such measurements were further applied with higher concentrations at 1 nM, 10 nM, 50 nM, 100 nM, 1000 nM, 1500 nM and 2000 nM of streptavidin. We find that the Dirac point shifts gradually as summarized in Table 1 in the supplementary information.

So the evolution of the Dirac point shift can be plotted. By applying the Langmuir–Freundlich formula to the Sips isotherm model (Murayama et al., 2024), the best fit to the curve of change in V_D versus streptavidin concentration can be obtained. Where ΔV_D is the voltage change due to the Dirac point shift from one streptavidin concentration with respect to the one measured with PBS, ΔV_m is the voltage change for the maximum shift of the Dirac point when the surface is saturated with streptavidin, C is streptavidin concentration, K_d is the Langmuir–Freundlich coefficient related to the equilibrium dissociation constant, and n is heterogeneous parameter between 0 and 1. This n value can vary depending on surface availability. If the surface is homogeneous (saturated), it fits the Langmuir model (n = 1), otherwise the Freundlich model is used for lower concentration (n < 1).

As a result, the dissociation constant K_d for streptavidin was found to be about 2.5 × 10^{-10} M for a maximum shift of the Dirac point ΔV_m

~ 0.27 V with an exponent n of about 0.41. The physical meaning of K_d is important because its value indicates the strength of the binding energy between streptavidin protein and biotin receptor. A higher K_d means a weaker interaction. Compared to the binding affinity of biotin–streptavidin widely accepted in solution ~ 10^{-14} M (Green, 1990), our findings are much larger as graphene in this work was covered with about 6 nm of CPA-PPF films exceeding the Debye screening length (less than 1 nm considered from the graphene surface (Murayama et al., 2024)) to justify this discrepancy. However, these results showed that the biotin grafted amines CPA-PPF/graphene can detect streptavidin protein by monitoring the shift of the Dirac point, and a fitting model was used to better predict the shift of the Dirac point away from the experimental data. The measured GFET with the graphene channel at the end of the experiments together with OM-SEM images taken after measuring 2000 nM streptavidin (see the supplementary Figure S9) shows very similar features with bright spots that may be the aggregation of streptavidin on some specific local surface areas as previously observed by confocal microscope.

To confirm that the shift of the Dirac point is due to interaction of streptavidin with the biotin on the graphene channel, confocal images of different fluorescent streptavidin concentrations were recorded in Figs. 6 (b-c). Obviously, a clear difference in fluorescence intensity is expected when comparing between 1 nM and 100 nM as well as 100 nM and 1000 nM (Fig. 6(b)). In fact, the maximum fluorescene intensity is at 1000 nM and it decreases about 3-fold at 100 nM and about 30-fold at 1 nM (see the supplementary Figure S10). However, it becomes more difficult to distinguish the fluorescent signal from the background below 1 nM. Therefore, a high sensitivity mode was applied to image the pM concentrations in Fig. 6(c). When taking a specific square area, the fluorescence intensities between streptavidin concentrations are almost the same and very slightly different from PBS, suggesting that fluorescent imaging was not sensitive enough to resolve the difference between samples with low streptavidin concentrations.

From the various experimental observations, the sensitivity of the Dirac point position to the presence of streptavidin in the LG-GFET channel is remarkable, especially at low concentrations. It is expected to improve further as the number of defects can be minimized, but that would require more time to investigate. More results measured on other GFET samples are also added to Supplementary Figure S11 to confirm the trend of such experiments. The goal of our study was to demonstrate the success of our functionalization strategy for the fabrication of sensitive biodetectors. This is why we used the well established biotin–streptavidin system. In future studies, it will be interesting to include non-specific proteins such as BSA (bovine serum albumine) to investigate to what extent specific target recognition is possible with our detectors.

4. Conclusions

The graphene surface on SiO_2/Si was functionalized with amino groups which is important for the immobilization of biotin bioreceptor. This was achieved by appropriately controlling the CPA polymerization. The uniformity of the polymerized CPA-coated graphene is confirmed by Raman mapping and the formation of covalent bonding between graphene and the CPA layer coatings as well as the presence of biotin on the surface are confirmed by XPS analysis. The surface morphology of graphene before and after CPA-PPF coatings and then, after biotin reaction is clearly evidenced by OM and SEM. Furthermore, fluorescent micrographs demonstrate the conjugation of fluorescent streptavidin with biotin grafted onto the amine-rich thin films/graphene LG-GFET devices. Electrical measurements show a shift of the Dirac point as a function of streptavidin concentration with a detection as low as 0.1 nM streptavidin.

Although the ability to detect streptavidin by our LG-GFET devices through biotin–streptavidin interaction has been demonstrated, further studies are still needed to measure the concentration of functional groups and of adsorbed molecules. Additionally, the detection of biomolecules with weaker binding to receptors than the streptavidin–biotin system will be investigated, as well as comparison of streptavidin with non-specific proteins and extention to other molecules of physiological interest such as antibodies, bacteria, etc.

CRediT authorship contribution statement

Trung T. Pham: Writing – original draft, Validation, Software, Project administration, Methodology, Conceptualization. **Jean-François Colomer:** Writing – review & editing, Formal analysis, Data curation. **José Ignacio Veytia-Bucheli:** Writing – review & editing, Resources, Formal analysis. **Benjamin Ledoux:** Writing – review & editing, Visualization, Validation, Software, Resources, Data curation. **Henri-François Renard:** Writing – review & editing, Software, Resources, Data curation. **Cédric R. Vandenabeele:** Writing – review & editing, Investigation, Formal analysis, Data curation. **Laurent A. Francis:** Writing – review & editing, Visualization, Validation, Software, Formal analysis. **Stéphane P. Vincent:** Writing – review & editing, Supervision, Resources, Formal analysis, Data curation. **Robert Sporken:** Writing – review & editing, Validation, Supervision, Methodology, Formal analysis, Conceptualization.

Declaration of competing interest

The authors declare no competing interests.

Acknowledgments

We gratefully acknowledge the financial support of NISM through the project: Graphene-based field-effect transistors for biodetection. Trung T. Pham would like to thank Jean-Pierre Van Roy for technical support, Xavier Delvaux for discussions on CPA plasma polymerization, Younes Bourenane Cherif for advice regarding the chemical method to functionalize graphene, Yves Caudano, Sarah-Davina Pierard and Xavier Maes for his FTIR supports, Nicolas Gros for Raman and Francesca Cecchet for Raman and AFM measurements. JFC is Senior Research Associate of the FRS-FNRS (Belgium). Use of the MORPH-IM, LOS, Electron Microscopy technological platforms of the UNamur for STM, AFM, Raman and SEM analysis is acknowledged.

Appendix A. Supplementary data

Supplementary material related to this article can be found online at https://doi.org/10.1016/j.biosx.2025.100673.

Data availability

Data will be made available on request.

References

Artemenko, A., Shchukarev, A., Stenclova, P., Wagberg, T., Segervald, J., Jia, X., Kromka, A., 2021. Reference XPS spectra of amino acids. IOP Conf. Ser.: Mater. Sci. Eng. 1050, 012001, https://iopscience.iop.org/article/10.1088/1757-899X/1050/1/012001.

Bartolomeo, A.D., Giubileo, F., Santandrea, S., Romeo, F., Citro, R., Schroeder, T., Lupina, G., 2011. Charge transfer and partial pinning at the contacts as the origin of a double dip in the transfer characteristics of graphene-based field-effect transistors. Nanotechnology 22, 275702, https://iopscience.iop.org/article/10.1088/0957-4484/22/27/275702.

Cai, B., Huang, L., Zhang, H., Z. Sun, Z., Zhang, G.-J., 2015. Gold nanoparticles-decorated graphene field-effect transistor biosensor for femtomolar MicroRNA detection. Biosens. Bioelectron. 74, 329–334. http://dx.doi.org/10.1016/j.bios.2015.06.068.

Cai, B., Wang, S., Huang, L., Ning, Y., Zhang, Z., Zhang, G.J., 2014. Ultrasensitive label-free detection of PNA-DNA hybridization by reduced graphene oxide field-effect transistor biosensor. ACS Nano 8, 2632–2638. http://dx.doi.org/10.1021/nn4063424.

Cançado, L.G., Jorio, A., Ferreira, E.H.M., Stavale, F., Achete, C.A., Capaz, R.B., Moutinho, M.V.O., Lombardo, A., Kulmala, T.S., Ferrari, A.C., 2011. Quantifying defects in graphene via Raman spectroscopy at different excitation energies. Nano Lett 11, 3190–3196. http://dx.doi.org/10.1021/nl201432g.

Cao, T.T., Nguyen, H.B., Nguyen, V.T., Vu, T.T., Bayle, M., Paillet, M., Sauvajol, J.L., Phan, B.T., Tran, D.L., Phan, N.M., Nguyen, V.C., 2018. An interdigitated ISFET-type sensor based on LPCVD grown graphene for ultrasensitive detection of carbaryl. Sensors Actuators B: Chem. 260, 78–85. http://dx.doi.org/10.1016/j.snb.2017.12.191.

Fu, W., Jiang, L., Geest E. P. van, L., Schneider, G.F., 2017. Sensing at the surface of graphene field-effect transistors. Adv. Mater. 29, 1603610. http://dx.doi.org/10.1002/adma.201603610.

Gao, Z. Rajesh, Vishnubhotla, R., Ducos, P., Serrano M. D, J., Robinson, M.K., Johnson, A.T.C., 2016. Genetically engineered antibody functionalized platinum nanoparticles modified CVD-graphene nanohybrid transistor for the detection of breast cancer biomarker. HER3. Adv. Mater. Interfaces 3, 1600124. http://dx.doi.org/10.1002/admi.201600124.

Geim, A.K., Novoselov, K.S., 2007. The rise of graphene. Nat. Mater. 6, 183–191. http://dx.doi.org/10.1038/nmat1849.

Georgakilas, V., Otyepka, M., Bourlinos, A.B., Chandra, V., Kim, N., Kemp, K.C., Hobza, P., Zboril, R., Kim, K.S., 2012. Functionalization of graphene: Covalent and non-covalent approaches. Deriv. Appl. Chem. Rev. 112, 6156–6214. http://dx.doi.org/10.1021/cr3000412.

Green, N.M., 1990. Avidin and streptavidin. Methods Enzymol. 184, 51–67. http://dx.doi.org/10.1016/0076-6879(90)84259-J.

Huang, Y., Sutter, E., Shi, N.N., Zheng, J., Yang, T., Englund, D., Gao, H.J., Sutter, P., 2015. Reliable exfoliation of large-area high-quality flakes of graphene and other two-dimensional materials. ACS Nano 9, 10612–10620. http://dx.doi.org/10.1021/acsnano.5b04258.

Jeon, S., Lee, J., Park, R., Jeong, J., Shin M. C, S.U., Park, J., Hong S. W, 2020. Graphene templated DNA arrays and biotin-streptavidin sensitive bio-transistors patterned by dynamic self-assembly of polymeric films confined within a roll-on-plate geometry. Nanomaterials 10 (1468), http://dx.doi.org/10.3390/nano10081468.

Kim, D.H., Oh, H.G., Park, W.H., Jeon, D.C., Lim, K.M., Kim, H.J., Jang, B.K., Song, K.S., 2018. Detection of alpha-fetoprotein in hepatocellular carcinoma patient plasma with graphene field-effect transistor. Sensors 18 (4032), http://dx.doi.org/10.3390/s18114032.

Liu, J., Tang, J., Gooding J. Justin, 2012. Strategies for chemical modification of graphene and applications of chemically modified graphene. J. Mater. Chem. 22, 12435–12452. http://dx.doi.org/10.1039/C2JM31218B.

Mohanty, N., Berry, V., 2008. Graphene-based single-bacterium resolution biodevice and DNA transistor: Interfacing graphene derivatives with nanoscale and microscale biocomponents. Nano Lett. 8, 4469–4476. http://dx.doi.org/10.1021/nl802412n.

Murayama, K., Furukawa, C., Yamasaki, S., Ohno, Y., Kajisa, T., Nagase, M., 2024. Biosensing beyond debye screening length using epitaxial graphene field-effect transistors on SiC substrate. Surfaces Interfaces 54, 105279. http://dx.doi.org/10.1016/j.surfin.2024.105279.

Myung, S., Solanki, A., Kim, C., Park, J., Kim, K.S., Lee, K.B., 2011. Graphene-encapsulated nanoparticle-based biosensor for the selective detection of cancer biomarkers. Adv. Mater. 23, 2221–2225. http://dx.doi.org/10.1002/adma.201100014.

Nam, J., Yang, J., Zhao, Y., Kim, K.S., 2024. Chemical vapor deposition of graphene and its characterizations and applications. Curr. Appl. Phys. 61, 55–70. http://dx.doi.org/10.1016/j.cap.2024.02.010.

Novodchuk, I., Bajcsy, M., Yavuz, M., 2021. Graphene-based field effect transistor biosensors for breast cancer detection: A review on biosensing strategies. Carbon 172 (431), http://dx.doi.org/10.1016/j.carbon.2020.10.048.

Ohno, Y., Maehashi, K., Yamashiro, Y., Matsumoto, K., 2009. Electrolyte-gated graphene field-effect transistors for detecting pH and protein adsorption. Nano Lett. 9, 3318–3322. http://dx.doi.org/10.1021/nl901596m.

Pham, T.T., Huynh, T.H., Colomer, J-F., Reckinger, N., Hackens, B., Sporken, R., 2025. Semi-dry transfer of CVD graphene on Si: surface morphology and electronic properties. Nanoscale 17, 11060–11070. http://dx.doi.org/10.1039/D4NR04986A.

Pourmadadi, M., Dinani, H.S., Tabar, F.S., Khassi, K., Janfaza, S., Tasnim, N., Hoorfar, M., 2022. Properties and applications of graphene and its derivatives in biosensors for cancer detection: A comprehensive review. Biosensors 12 (269), http://dx.doi.org/10.3390/bios12050269.

Ravi, S., Zhang, S., Lee, Y.-R., Kang, K.-K., Kim, J.-M., Ahn, J.-W., Ahn, W.-S., 2018. EDTA-functionalized KCC-1 and KIT-6 mesoporous silicas for Nd 3+ ion recovery from aqueous solutions. J. Ind. Eng. Chem. 67, 210–218. http://dx.doi.org/10.1016/j.jiec.2018.06.031.

Shown, I., Ganguly, A., 2016. Non-covalent functionalization of CVD-grown graphene with au nanoparticles for electrochemical sensing application. J. Nanostructure Chem. 6, 281–288. http://dx.doi.org/10.1007/s40097-016-0201-6.

Vesel, A., Zaplotnik, R., Primc, G., Mozetic, M., 2020. A review of strategies for the synthesis of N-doped graphene-like materials. Nanomaterials 10 (2286), http://dx.doi.org/10.3390/nano10112286.

Wan, Q., Han, L., Guo, Y., Yu, H., Tan, L., Zheng, A., Chen, Y., 2021. Graphene-based biosensors with high sensitivity for detection of ovarian cancer cells. Molecules 26 (7265), http://dx.doi.org/10.3390/molecules26237265.

Wang, Y.-Y., Burke, P.J., 2013. A large-area and contamination-free graphene transistor for liquid-gated sensing applications. Appl. Phys. Lett. 103, 052103. http://dx.doi.org/10.1063/1.4816764.

Xu, S., Jiang, S., Zhang, C., Yue, W., Zou, Y., Wang, G., Liu, H., Zhang, X., Li, M., Zhu, Z., Wang, J., 2018. Ultrasensitive label-free detection of DNA hybridization by sapphire-based graphene field-effect transistor biosensor. Appl. Surf. Sci. 427, 1114–1119. http://dx.doi.org/10.1016/j.apsusc.2017.09.113.

Yan, L., Zheng, Y.B., Zhao, F., Li, S., Gao, X., Xu, B., Weiss, P.S., Zhao, Y., 2012. Chemistry and physics of a single atomic layer: strategies and challenges for functionalization of graphene and graphene-based materials. Chem. Soc. Rev. 41, 97–114. http://dx.doi.org/10.1039/C1CS15193B.

Zhou, L., Mao, H., Wu, C., Tang, L., Wu, Z., Sun, H., Zhang, H., Zhou, H., Jia, C., Jin, Q., Chen, X., Zhao, J., 2017. Label-free graphene biosensor targeting cancer molecules based on non-covalent modification. Biosens. Bioelectron. 87, 701–707. http://dx.doi.org/10.1016/j.bios.2016.09.025.